remote sensing

MDPI

Article

Long-Term Assessment of UHI and SUHI in Modena: Integrating Landsat Land Surface Temperature and Meteorological Observations

Stephanie Vega Parra [1,2,*], Francesca Despini [2], Sofia Costanzini [2], José Antonio Sobrino [3], Lucas De la Fuente Daruich [4] and Sergio Teggi [2]

1 University School for Advanced Studies IUSS Pavia, 27100 Pavia, Italy
2 Department of Engineering "Enzo Ferrari", University of Modena and Reggio Emilia, 41125 Modena, Italy; francesca.despini@unimore.it (F.D.); sofia.costanzini@unimore.it (S.C.); sergio.teggi@unimore.it (S.T.)
3 Global Change Unit (UCG), Image Processing Laboratory (IPL), University of Valencia, 46980 Paterna, Spain; jose.sobrino@uv.es
4 Orbital, 46980 Paterna, Spain; lucas@orbitaleos.com
* Correspondence: stephanie.vegaparra@iusspavia.it; Tel.: +39-059-205-6203

Highlights

What are the main findings?

- Summer daytime land surface temperatures (LST) increased by approximately 10 °C between 1985 and 2023 across both urban and rural areas of Modena.
- Nighttime land surface and air temperatures closely agree, whereas daytime relationships are much weaker.

What are the implications of the main findings?

- Nighttime satellite images best capture near-surface air warming; daytime images best characterize the surface urban heat island (SUHI) itself.
- Combining satellite and ground data is key to understanding and managing heat in medium-sized cities.

Abstract

The urban heat island (UHI) refers to higher air temperatures (T_{air}) in urban areas than in surrounding rural environments, while the surface urban heat island (SUHI) describes analogous differences in land surface temperature (LST). This study presents a long-term assessment of UHI and SUHI in Modena, Italy, combining meteorological T_{air} observations with Landsat-derived LST from 188 daytime and 19 nighttime summer scenes (1985–2023). Four indicators—magnitude and range 1 of overall thermal variability and magnitude and range 2 of urban–rural thermal excess—were applied in parallel to LST and T_{air} to characterize the intensity and spatial variability of thermal conditions within a consistent daytime/nighttime framework. Results indicate significant long-term increases in summer LST, with daytime warming rates of 0.26 °C yr^{-1} (urban) and 0.27 °C yr^{-1} (rural). Daytime urban–rural LST differences ranged from 4 to 6 °C; nighttime differences were smaller (1–3 °C). Daytime T_{air} urban–rural differences were weak and not statistically significant, whereas nighttime T_{air} showed a clearer urban warming signal. Nighttime LST correlated more closely with T_{air} (r = 0.49–0.52 across indicators) than daytime LST, and nighttime LST showed strong correlations with T_{air} in both urban and rural areas (r = 0.96–0.98). Daytime imagery better captures SUHI spatial intensity, whereas nighttime observations provide a more consistent surface-to-atmosphere thermal link, highlighting the value of integrating satellite LST with in situ T_{air} for integrated UHI and SUHI assessment in medium-sized cities.

Academic Editor: Jiayi Li

Received: 15 June 2026
Revised: 2 August 2026
Accepted: 5 August 2026
Published: 10 August 2026

Keywords: surface urban heat island; urban heat islands; remote sensing; land surface temperature (LST); indicators

1. Introduction

The urban heat island (UHI) is a phenomenon affecting thousands of cities worldwide, characterized by higher air temperatures (T_{air}) in urban areas than in their surrounding rural counterparts [1]. This thermal disparity has significant implications for public health and well-being [1,2]. UHI intensity is typically evaluated using T_{air} measurements from meteorological stations and is most pronounced at night, when urban surfaces release the heat accumulated throughout the day [3]. In contrast, the surface urban heat island (SUHI) is based on land surface temperatures (LST) retrieved from satellite imagery. It typically shows stronger urban–rural contrasts in the late morning or afternoon due to solar radiation absorption [4,5], although it can also emerge in the evening depending on material properties and local meteorological conditions [6].

Urbanization is one of the principal drivers of both UHI and SUHI [7,8]. Dense built-up areas, extensive impervious surfaces, reduced vegetation cover, and the high heat storage capacity of urban materials enhance sensible heat storage while limiting evaporative cooling, thereby increasing urban temperatures [5,9,10]. The intensity of these effects depends on the thermal conductivity, net radiation, and turbulent heat fluxes of urban surfaces which govern how energy is exchanged and stored within the urban environment [11–15]. These processes are particularly pronounced in hot arid and semi-arid cities such as Tehran, Riyadh, and desert cities in Arizona [16–18].

Although most UHI and SUHI studies have focused on large metropolitan areas, recent research demonstrates that medium-sized cities can also experience significant urban thermal anomalies despite receiving comparatively less scientific attention [19,20]. In Italy, for example, Padua has been explicitly described as a medium-sized city affected by a marked UHI (7 °C) [21], while Bari has also shown clear urban thermal contrasts in a Mediterranean context [20]. Within the Po Valley, Modena is a particularly valuable case study owing to its fragmented urban development, limited atmospheric ventilation, and frequent stable atmospheric conditions associated with the basin topography, which have also been linked to recurrent air quality issues in the area [22]. The increasing occurrence of summer heatwaves further compounds these conditions [23–25]. Previous studies have documented daytime SUHI differences of up to 6.4 °C in the city [23], with urbanization contributing up to 65% of the increase in warm nights in recent decades [26], making Modena well suited for investigating the long-term relationship between UHI and SUHI.

Integrating in situ T_{air} and satellite LST provides a comprehensive assessment by capturing both atmospheric and surface thermal patterns [4,27,28]. However, because T_{air} and LST represent different components of the urban environment, UHI and SUHI intensity estimates are not directly equivalent [29]. For example, Tomlinson et al. (2012) [12] reported that MODIS observations tend to underestimate nighttime SUHI intensity compared with T_{air} measurements. Likewise, Yang et al. (2020) [30] reported that LST-based SUHI can be considerably stronger than atmospheric UHI, with summer daytime differences reaching 6.83 °C compared with only 0.27 °C based on T_{air}. Sheng et al. (2017) [31] similarly observed summer differences of 5–8 °C between LST and T_{air}-derived SUHI estimates.

These methodological differences highlight the importance of carefully defining urban and rural reference areas and selecting appropriate UHI indicators [31]. Although previous studies have compared T_{air} and LST [29], relatively few have performed parallel long-term analyses using both meteorological observations and satellite data over the same city and period, particularly for medium-sized cities.

To address this gap, the present study performs a parallel long-term assessment of UHI and SUHI in Modena (Italy), based on meteorological station T_{air} observations and Landsat-derived LST spanning more than three decades, using four complementary indicators. Specifically, the objectives are to: (i) assess daytime and nighttime UHI and SUHI patterns; (ii) quantify their spatial and temporal variability; and (iii) investigate the statistical relationships between atmospheric and surface thermal indicators.

2. Materials and Methods

2.1. Study Area

Modena is located in the Emilia-Romagna region of northern Italy, within the Po Valley, a highly anthropized region characterized by a mosaic of urban development, agricultural land, livestock activities, and industrial areas [26]. The climate is warm temperate with continental influence (Cfa, Köppen–Geiger) [32], with hot summers and frequent drought episodes in July–August, occasionally interrupted by intense thunderstorms [22]. Modena represents a medium-sized urban context (184,739 inhabitants) [33].

UHI assessment was based on T_{air} measurements from five meteorological stations (one urban and four rural), while SUHI assessment used satellite-derived LST. Five circular buffers (radius: 500 m) were delineated around the stations to compare point-based T_{air} with spatially averaged LST representative of the surrounding environment [34].

A preliminary assessment of LST spatial patterns was conducted by classifying the study area into urban and rural areas. Urban and rural areas were defined using land cover data from the European Space Agency (ESA) Climate Change Initiative (CCI) Land Cover project [35], widely adopted to delineate urban extent in UHI studies [36]. This classification supports the comparison of urban and rural temperature conditions across the study period. Figure 1 shows the meteorological stations, the 500 m buffers, and the urban and rural areas.

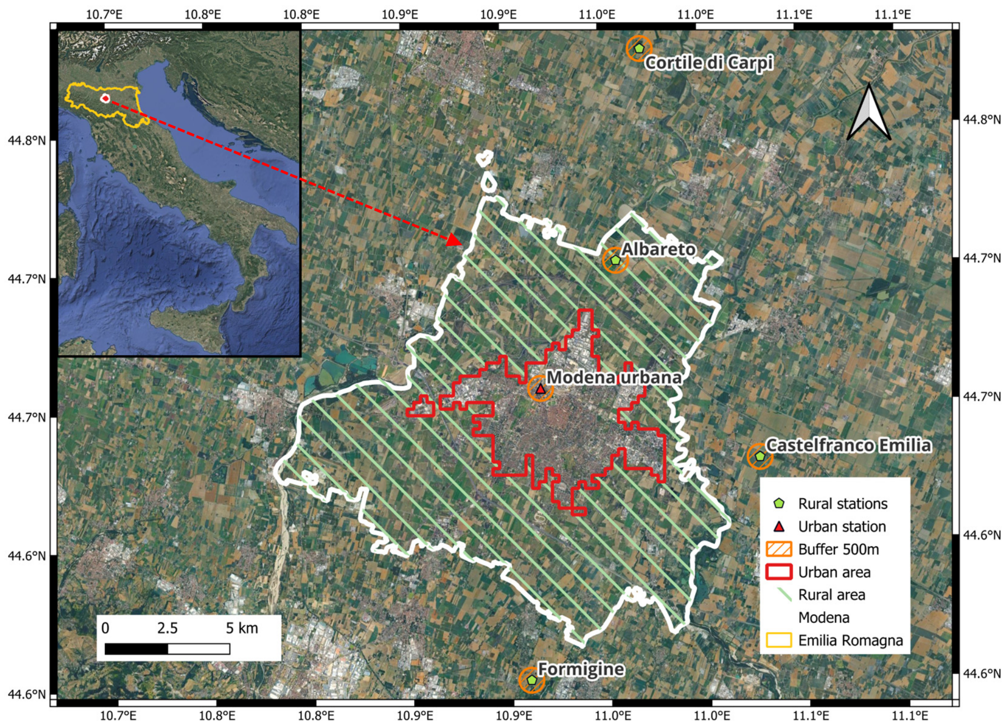

Figure 1. Study area in Modena, Italy.

2.2. Data Sources

The temporal analysis integrated LST derived from Landsat satellite imagery with T_{air} obtained from meteorological observations. The Landsat archive has provided consistent Earth observation data since 1972, with thermal bands calibrated across missions and resampled to a spatial resolution of 30 m.

2.2.1. Landsat Data—Daytime and Nighttime Images

Landsat imagery was obtained from the United States Geological Survey (USGS) Earth Resources Observation and Science (EROS) Center and accessed via Google Earth Engine (GEE) for large-scale dataset processing, as in previous studies [37–40].

Landsat Collection 2, Level 2, Tier 1 products were used, providing atmospherically corrected LST data with high geometric quality [41,42]. Daytime scenes were selected after quality screening. Images with more than 20% cloud cover were excluded, while cloud, cloud shadow, cirrus, and radiometrically saturated pixels were removed using the quality assessment (QA) mask. Following QA masking, only scenes retaining at least 80% valid pixels were included in the analysis. In addition, Landsat 7 scenes acquired after the 2003 Scan Line Corrector (SLC) failure were excluded because the resulting data gaps reduce image coverage and may affect the analysis [43,44].

Table 1 summarizes the Landsat collections and the number of daytime scenes. Landsat overpasses the study area between approximately 09:45 and 10:05 UTC, with a nominal revisit interval of 16 days.

Table 1. Number of daytime Landsat images after filtering on the GEE platform.

Collection in GEE	Time Period Evaluated	Availability (No. Images)
LANDSAT/LT05/C02/T1_L2	2 May 1985 to 17 October 2011	235
LANDSAT/LC08/C02/T1_L2	7 June 2013 to 26 November 2023	167

Nighttime Landsat acquisitions are limited because routine observations are primarily scheduled during the morning descending overpass, while nighttime (ascending) scenes are only collected upon specific acquisition request. Nighttime images were obtained from Collection 2, Tier 2 top-of-atmosphere (TOA) products. Since TOA products for nighttime acquisitions do not provide a reliable cloud cover estimate [45,46], all scenes were visually inspected, and only cloud-free images were retained [47,48]. Table 2 summarizes the selected nighttime scenes. The satellite passed over Modena at approximately 20:15–20:30 UTC for Landsat 5 and 20:50–21:00 UTC for Landsat 8/9.

Table 2. Number of nighttime Landsat images after filtering.

Collection in GEE	Time Period Evaluated	Availability (No. Images)
LANDSAT/LT05/C02/T2_TOA	6 December 1985 to 9 October 1991	5
LANDSAT/LC08/C02/T2_TOA	9 September 2014 to 25 September 2023	43
LANDSAT/LC09/C02/T2_TOA	31 July 2023 to 17 September 2023	3

The final daytime dataset comprised 402 Landsat images acquired between 1985 and 2023. Temporal coverage was provided by Landsat 5 until 2011 and Landsat 8 from 2013 onward; no suitable images were available for 2002 or 2012. Of these, 188 summer images (June–August) were used in this analysis. The final nighttime dataset comprised 19 cloud-free summer images from 1991, 2015, 2018, 2019, and 2023.

2.2.2. Meteorological Data

The meteorological data from urban and rural stations were extracted using the Dext3r application. Dext3r is a platform that allows the extraction of weather data recorded by the regional monitoring network managed by Arpae-Simc [49]. The hourly mean T_{air} data at 2 m above ground level were extracted, starting from the earliest available year in the archive.

All data are provided in UTC, meaning that the time difference with local Italian time is one hour during standard time (winter period) and two hours during daylight saving time (summer period). In this study, the UTC format, in accordance with Landsat data, was used for both daytime and nighttime evaluations. The characteristics of the weather stations are described in Table 3.

Table 3. Meteorological stations characteristics [49].

Station	Location	Municipality	Height (MASL)	Longitude	Latitude	U.M	Start Year	End Year
Albareto	Rural	Modena	28	10.956703	44.702144	°C	2001	2023
Castelfranco Emilia	Rural	Castelfranco Emilia	32	11.027469	44.630051	°C	2001	2023
Cortile di Carpi	Rural	Carpi	23	10.971285	44.778387	°C	2007	2023
Formigine	Rural	Formigine	90	10.909373	44.551227	°C	2004	2023
Modena Urbana	Urban	Modena	73	10.916985	44.656392	°C	2005	2023

2.3. Data Processing and Analysis Methods

The methodological workflow adopted in this study is summarized in Figure 2. It includes the main processing steps from data processing to the calculation of the UHI and SUHI metrics.

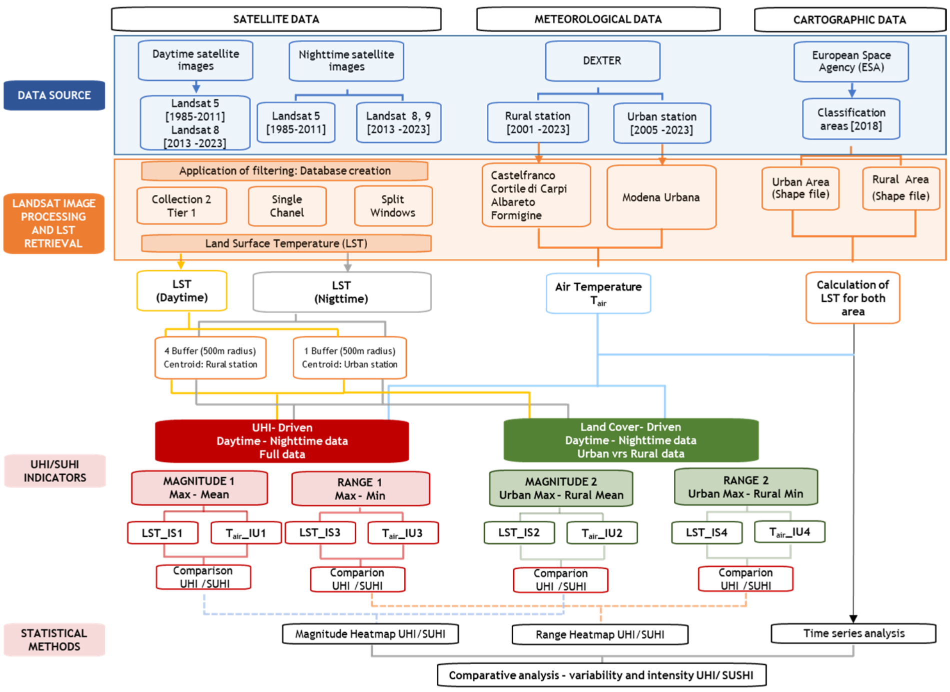

Figure 2. Methodological workflow for daytime and nighttime LST processing, T_{air} extraction, and UHI/SUHI indicator analysis.

2.3.1. Landsat Image Processing and LST Retrieval

Daytime LST analyses were based on Landsat Collection 2, Level 2. These products are generated using the processing workflow described in [41,42], which integrates thermal infrared (TIR) bands, surface emissivity, vegetation indices, and atmospheric profiles from the Goddard Earth Observing System (GEOS-IT, 2024–present), Forward Processing for Instrument Teams (FP-IT, 2000–2023), and Modern-Era Retrospective Analysis for Research and Applications (MERRA-2, 1982–1999). Optical bands were converted to surface reflectance and thermal bands to LST using the mission-specific scaling coefficients.

To retrieve nighttime LST from Landsat 5 thermal data, a single-channel (SC) approach was applied [50,51]. Surface-emitted radiance was estimated by correcting the at-sensor radiance for atmospheric transmission, upwelling/downwelling radiance, and surface emissivity using the radiative transfer equation (RTE) (Equation (1)).

$$B(T_s) = \frac{L_{sen} - L\uparrow - \tau(1-\varepsilon)L\downarrow}{\tau\varepsilon} \tag{1}$$

where

$B(T_s)$: blackbody radiance corresponding to the surface temperature T_s;
L_{sen}: at-sensor radiance measured by the satellite in the thermal band (top-of-atmosphere radiance);
$L\uparrow$: upwelling atmospheric radiance;
$L\downarrow$: downwelling atmospheric radiance;
τ: atmospheric transmittance;
ε: surface emissivity.

Surface emissivity (ε) was estimated from the closest available daytime Landsat image to each nighttime acquisition, assuming limited short-term variability in emissivity for urban surfaces, as supported by previous studies reporting only minor day–night emissivity differences under stable surface conditions [52]. Atmospheric inputs (pressure and water vapor) were taken from ERA5 (ECMWF Reanalysis v5) profiles produced by the European Centre for Medium-Range Weather Forecasts (ECMWF) and used in the Moderate Resolution Atmospheric Transmission (MODTRAN) radiative transfer model to compute atmospheric transmittance and upwelling/downwelling radiance required by the radiative transfer equation. The corrected radiance was converted to LST by inverting the Planck function using the sensor-specific calibration constants (Equation (2)).

$$T_s = \frac{K_2}{l_n\left(\frac{k_1}{B(T_s)} + 1\right)} \tag{2}$$

where

T_s: land surface temperature (K);
$B(T_s)$: blackbody radiance corresponding to the surface temperature T_s, as defined in Equation (1);
K_1: 607.76 ($W{\cdot}m^{-2}{\cdot}sr^{-1}{\cdot}\mu m^{-1}$);
K_2: 1260.56 K.

Nighttime LST from Landsat 8 was retrieved using the split-window (SW) algorithm proposed by Jiménez-Muñoz et al. (2014) [53], Equation (3), which exploits the two TIR bands in the atmospheric window (10–12 µm). The method estimates LST by combining the at-sensor brightness temperatures of the two thermal bands and correcting for surface emissivity and atmospheric water vapor.

$$T_s = T_i + c_1(T_i - T_j) + c_2(T_i - T_j)^2 + c_0 + (c_3 + c_4 w)(1 - \varepsilon) + (c_5 + c_6 w)\Delta\varepsilon \quad (3)$$

where

T_s: land surface temperature (K);
T_i, T_j: at-sensor brightness temperatures in the two split-window thermal bands i and j (K);
ε: mean surface emissivity of the two bands, computed as the average of εi and εj;
$\Delta\varepsilon$: emissivity difference between the two bands (εi − εj);
w: total atmospheric water vapor content (g·cm^{-2});
c_0–c_6: split-window regression coefficients (sensor/algorithm-specific) derived from statistical fitting on simulated datasets (typically generated with MODTRAN using atmospheric profiles).

The coefficients adopted in this study were: (c_0 = −0.268), (c_1 = 1.378), (c_2 = 0.183), (c_3 = 54.30), (c_4 = −2.238), (c_5 = −129.20), and (c_6 = 16.40) [53]. Water vapor content (w) was obtained from ERA5 and cross-checked against available Italian radiosonde observations from the station closest to Modena.

2.3.2. UHI and SUHI Indicators

UHI and SUHI intensity and spatial variability were characterized using four indicators adapted from previous studies [31,54]. Two groups of indicators were considered: (i) UHI-driven indicators, based on the overall thermal variability among all buffers/stations, and (ii) land cover-driven indicators, explicitly comparing urban and rural conditions. The equations corresponding to these four indicators are presented in Table 4. LST-based indicators were derived from Landsat daytime (10:00 UTC) and nighttime (21:00 UTC) acquisitions for the period 1985–2023. Mean, maximum, and minimum LST values were extracted within five buffers centered on the meteorological stations.

Table 4. Surface urban heat island (SUHI) and urban heat island (UHI) indicators for land surface temperature (LST) and air temperature (T_{air}) implemented for this study and derived by [31,54].

Category	Indicator	SUHI LST_IS: Indicator by Using LST Landsat	UHI T_{air}_IU: Indicator by Using Meteorological Station
UHI-driven	Magnitude 1	LST_IS1 = $\mathrm{Max}(\mathrm{LST}_5*) - \mathrm{Mean}(\mathrm{LST}_5*)$	T_{air}_IU1 = $\mathrm{Max}(T_{air5}*) - \mathrm{Mean}(T_{air5}*)$
Land cover-driven	Magnitude 2	LST_IS2 = Max(LST_urban) − Mean(LST_rural$_4*$)	T_{air}_IU2 = Max(T_{air}_urban) − Mean(T_{air}_rural$_4*$)
UHI-driven	Range 1	LST_IS3 = $\mathrm{Max}(\mathrm{LST}_5*) - \mathrm{Min}(\mathrm{LST}_5*)$	T_{air}_IU3 = $\mathrm{Max}(T_{air5}) - \mathrm{Min}(T_{air5}*)$
Land cover-driven	Range 2	LST_IS4 = Max(LST_urban) − Min(LST_rural$_4*$)	T_{air}_IU4 = Max(T_{air}_urban) − Min(T_{air}_rural$_4*$)

Note: (*) indicates the number of buffers/stations.

T_{air}-based indicators were computed using hourly observations from five meteorological stations, considering only dates corresponding to Landsat overpasses to ensure temporal consistency.

UHI-driven indicators (Magnitude 1 and Range 1) describe thermal variability across all buffers/stations, whereas land cover-driven indicators (Magnitude 2 and Range 2) quantify the maximum urban thermal excess relative to rural conditions.

All LST indicators were calculated separately for daytime and nighttime datasets. T_{air} indicators were computed hourly for the same acquisition dates, enabling direct comparison between SUHI and UHI intensity.

2.3.3. Statistical Methods

The relationship between LST and T_{air} indicators was examined using cross-correlation analysis. The time series analyzed were:

1. Indicator IS derived from LST at 10:00 UTC;
2. Indicator IU obtained from hourly T_{air} from meteorological ground stations (from 00:00 to 23:00 UTC).

The first series was iteratively compared with the second for each hour of the day, resulting in 24 correlation values, one for each hour, computed for all common dates between Landsat and meteorological data.

The Pearson correlation coefficient was used to measure the strength of the relationship between the variables. Additionally, a statistical approach based on Student's t-distribution was applied to compute confidence intervals and assess significance. Specifically, a two-tailed *t*-test was used to evaluate statistical significance at the 95% confidence level, and the *p*-value was computed accordingly to estimate the likelihood of the observed correlation under the null hypothesis. To construct confidence intervals for each correlation value, the Fisher z-transformation (z = arctanh(r)) was applied to normalize the distribution of r. The resulting interval was then converted back to the correlation scale using the inverse hyperbolic tangent function. Finally, heatmaps were used to enhance the visualization of correlations between Landsat-derived and meteorological variables across different hours of the day.

3. Results

3.1. Urban–Rural LST Patterns

The spatial distribution of mean daytime summer LST was analyzed at five-year intervals from 1985 (Figure 3). In all daytime and nighttime maps, the solid line indicates the study area boundary, while the circles represent buffer zones around the weather stations.

Mean daytime summer LST maps reveal a persistent urban warm core surrounded by cooler rural areas. The spatial extent of higher LST values increased in the most recent years, indicating an overall warming of the study area.

Nighttime LST exhibited spatial patterns similar to those observed during the daytime, with consistently higher LST in the urban area than in the surrounding rural areas (Figure 4).

Absolute temperatures were considerably lower, ranging from approximately 15 °C to 28 °C, whereas daytime LST reached about 50 °C. Among the selected years, 2015 exhibited particularly high daytime and nighttime LST values, consistent with the summer heatwave that affected Italy and large parts of Europe [55,56]. These patterns are analyzed in more detail in the time series presented below.

3.2. Daytime and Nighttime LST Time Series

Daytime values represent the annual mean calculated from all available summer Landsat images, whereas each nighttime observation corresponds to a single available summer image, as shown in Figures 5 and 6, respectively.

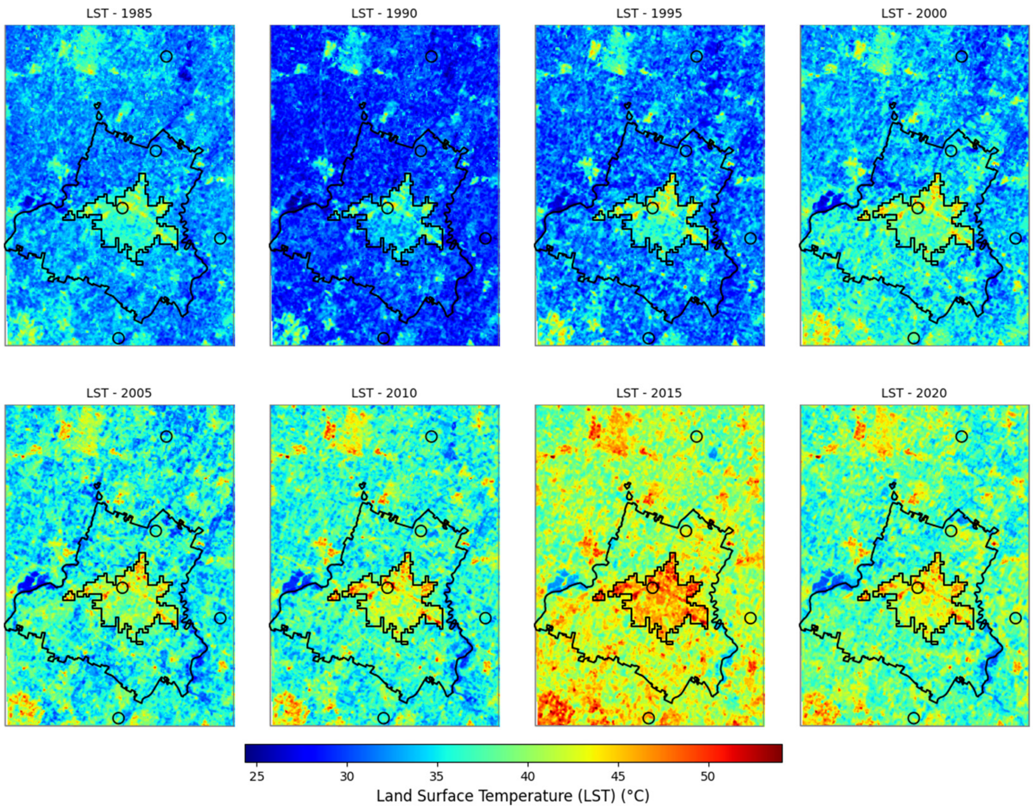

Figure 3. Mean daytime summer LST for selected years (1985–2023) over the study area.

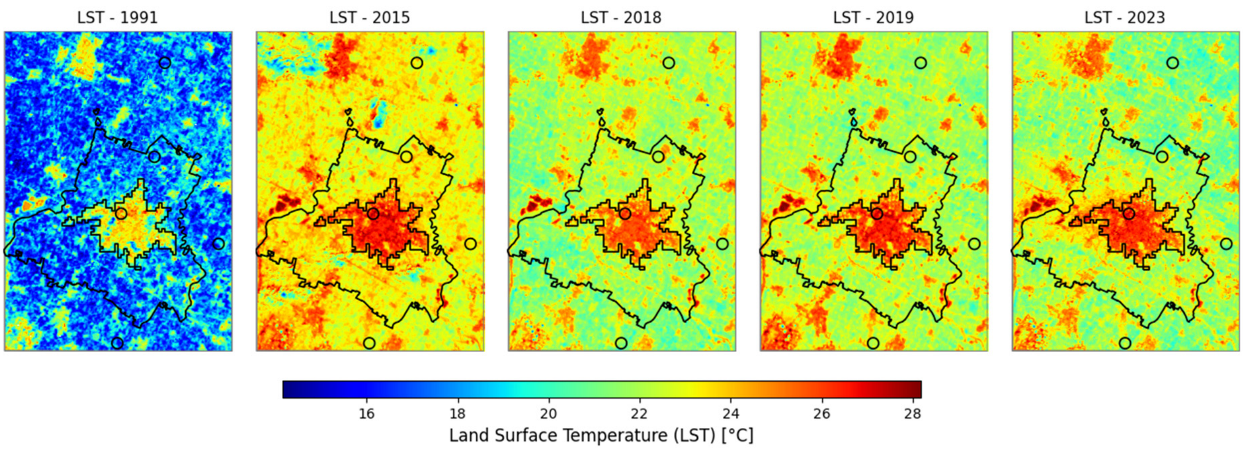

Figure 4. Mean nighttime summer LST for 1991, 2015, 2018, 2019, and 2023 over the study area.

The results show a statistically significant increase in summer LST, with a linear trend of 0.27 ± 0.03 °C yr^{-1} in the rural area and 0.26 ± 0.02 °C yr^{-1} in the urban area. These trends are supported by 95% confidence intervals (CI) [~0.21 to 0.33 °C yr^{-1}] and highly significant p-values ($\ll$0.001), indicating a robust LST increase over the study period. The cumulative increase in mean summer LST is approximately 10 °C over four decades (0.26 °C yr^{-1}), as estimated from the linear trend of the urban and rural series. During summer daytime conditions, the urban–rural LST difference is approximately 4–6 °C.

Nighttime LST observations also remained consistently higher in the urban area, although the urban–rural difference was smaller (approximately 1–3 °C). Both series exhibited an overall increase, with a pronounced peak in 2015, corresponding to the exceptional summer heatwave previously identified in Figure 4.

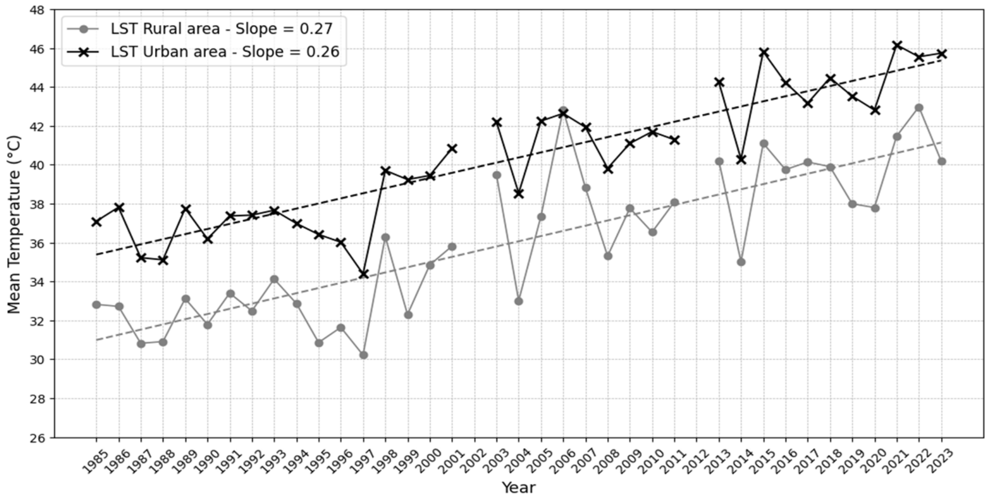

Figure 5. Summer daytime LST trends for the urban and rural areas (1985–2023).

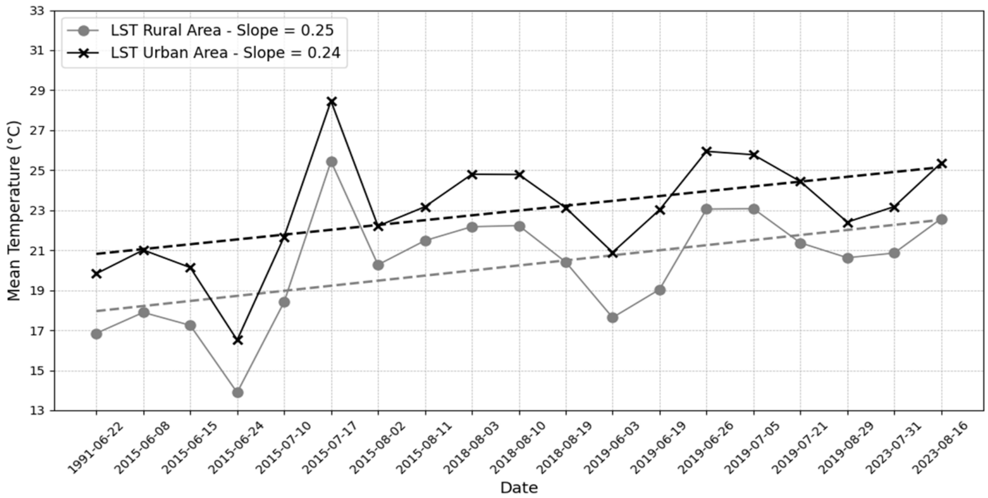

Figure 6. Summer nighttime LST observations for the urban and rural areas.

3.3. Daytime and Nighttime T_{air} Time Series

Daytime values represent the annual mean calculated from measurements acquired on the same dates as the available daytime Landsat images, whereas each nighttime observation corresponds to the measurement recorded on the date of a nighttime Landsat acquisition, as shown in Figures 7 and 8, respectively.

During daytime, mean T_{air} was slightly higher at the rural stations than at the urban station, with differences ranging from approximately 0.2 to 1.0 °C (Figure 7). Linear trends for 2005–2023 were +0.03 °C yr^{-1} in the rural series and +0.06 °C yr^{-1} in the urban series, although neither trend was statistically significant ($p > 0.05$). Both series exhibited substantial interannual variability and a pronounced peak in 2015.

Nighttime T_{air} observations (2015–2023) also showed increasing temperatures in both the urban and rural series (Figure 8). Estimated trends were +0.26 °C yr^{-1} for the urban station and +0.23 °C yr^{-1} for the rural stations. The urban trend was statistically significant ($p = 0.039$), whereas the rural trend was marginally non-significant ($p = 0.060$).

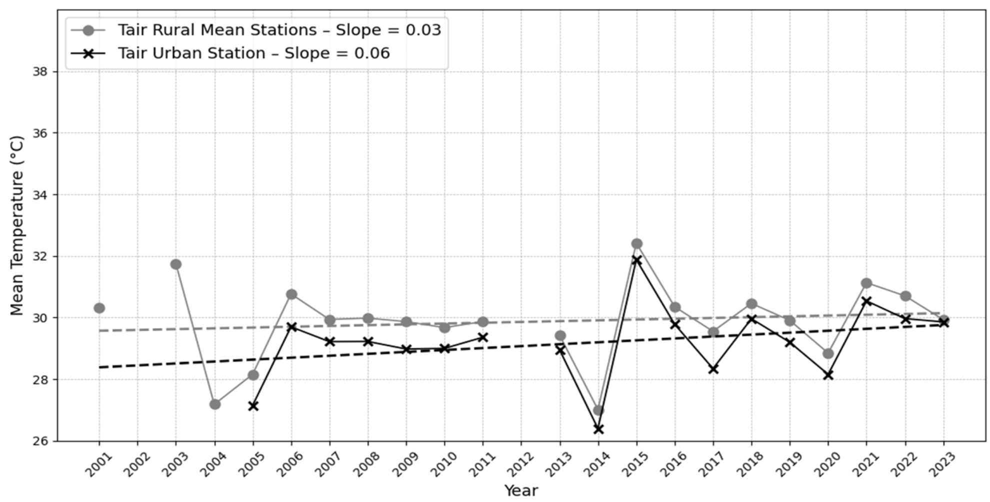

Figure 7. Summer daytime T_{air} series for the urban station and the mean of the four rural stations (2005–2023).

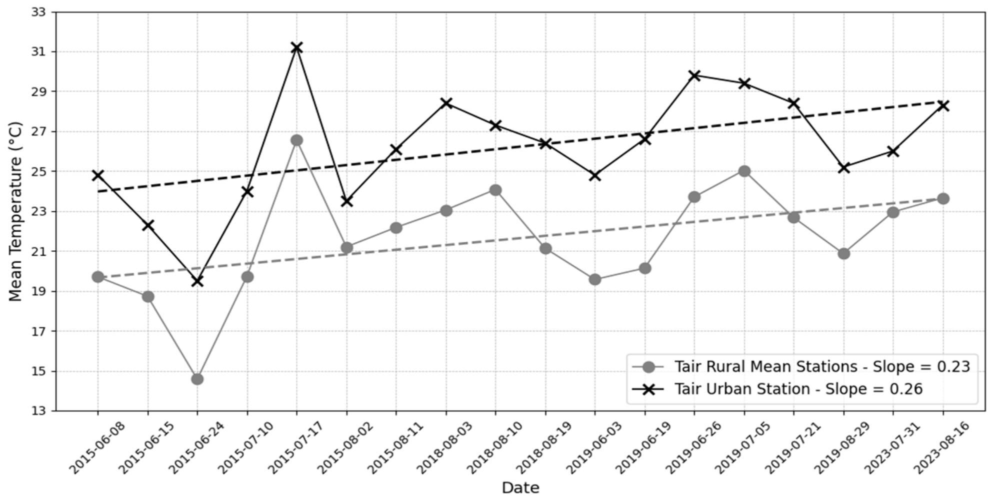

Figure 8. Summer nighttime T_{air} observations for the urban station and the mean of the four rural stations (2015–2023).

3.4. Comparison of Nighttime LST and T_{air}

LST was derived from Landsat nighttime images, whereas T_{air} was measured at the corresponding acquisition times by the Modena Urbana station and the mean of the four rural stations, as shown in Figure 9 for the urban and rural areas.

Between 2015 and 2023, nighttime LST and T_{air} exhibited similar temporal behavior in both the urban and rural areas (urban area: slope = 0.24 °C yr^{-1}, p = 0.029; rural area: slope = 0.25 °C yr^{-1}, p = 0.024). Both LST trends were statistically significant at the 95% confidence level (95% CI: [0.028, 0.454] and [0.038, 0.469], respectively). Although three of the four rural meteorological stations are located outside the area used for the LST calculations, both variables showed a strong agreement. Correlation coefficients ranged from 0.96 in the urban area to 0.98 in the rural area ($p < 0.001$ in both cases), indicating a robust correspondence between satellite-derived LST and near-surface air temperature during nighttime. In contrast, the linear trends of the station-based T_{air} series (urban station and rural station) were not statistically significant over this shorter period, likely reflecting the smaller sample size and higher interannual variability of the ground-based records.

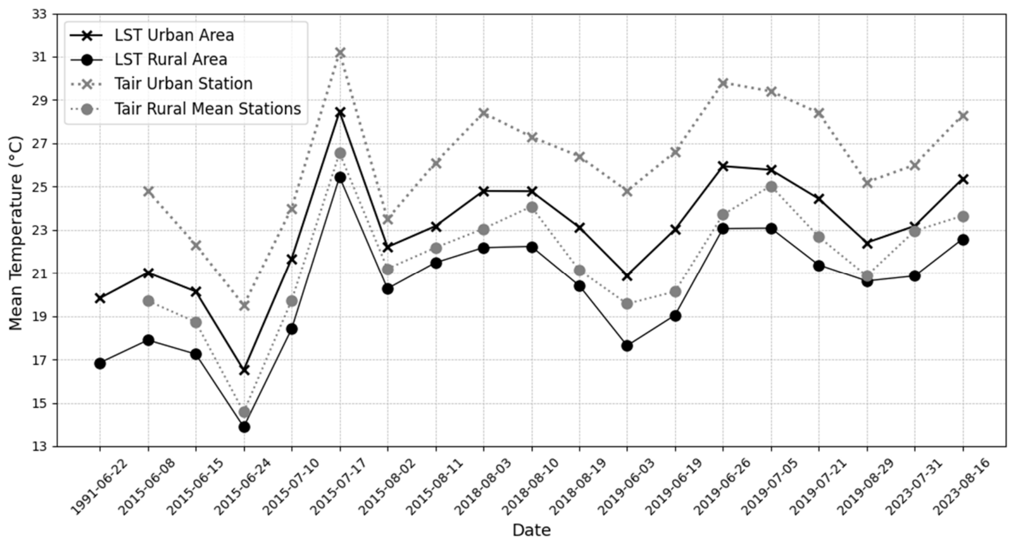

Figure 9. Comparison of nighttime LST and T_{air} for the urban and rural areas using coincident observations.

3.5. UHI and SUHI Intensity

Daytime indicator values are compared in Figure 10 and nighttime indicator values in Figure 11.

Magnitude daytime indicators (Figure 10a,b) consistently show much larger values for LST than for T_{air}. LST-based indices commonly ranged between approximately 10 and 25 °C, with peaks exceeding 24 °C during the 2015 and 2018 heatwaves, whereas T_{air}-based indices generally remained below 4 °C. These differences indicate that urban surfaces respond more rapidly and intensely to daytime solar heating than the near-surface air.

Range daytime indicators (Figure 10c,d) show a similar behavior. LST frequently exhibited spatial ranges exceeding 20–30 °C, occasionally reaching 37 °C, whereas T_{air} generally varied between 2 and 3 °C, with only occasional peaks approaching 4 °C. These findings highlight the greater spatial thermal variability of surface temperature compared with air temperature during daytime conditions.

Magnitude 1 and Magnitude 2 (Figure 11a,b) showed similar nighttime behavior. LST generally ranged from 3 to 6 °C in Magnitude 1 and Magnitude 2, with peaks approaching 6.5 °C. T_{air} exhibited comparable and occasionally higher values, with the largest urban–rural differences occurring on some nights after the Landsat overpass, indicating that nighttime atmospheric temperature differences can equal or exceed those at the surface.

Range 1 (Figure 11c) generally showed higher LST values than T_{air}. On two nights (8 June 2015 and 19 June 2019), however, this pattern was markedly amplified, with the LST–T_{air} gap reaching approximately 14 °C—well above the typical range—coinciding with the onset of summer heatwaves.

Range 2 (Figure 11d) showed LST values generally between 4 and 8 °C, whereas T_{air} ranged from 4 to 10 °C. On several nights, T_{air} exceeded the corresponding LST values, indicating that nighttime urban–rural temperature differences were sometimes larger in the atmosphere than at the surface.

3.6. Cross-Correlation Between UHI and SUHI Indicators

Cross-correlation heatmaps are presented in Figure 12. Panels (a) and (b) show the daytime results for the magnitude and range indicators, respectively, whereas panels (c) and (d) present the corresponding nighttime results. Warmer colors indicate positive correlations, and cooler colors indicate negative correlations.

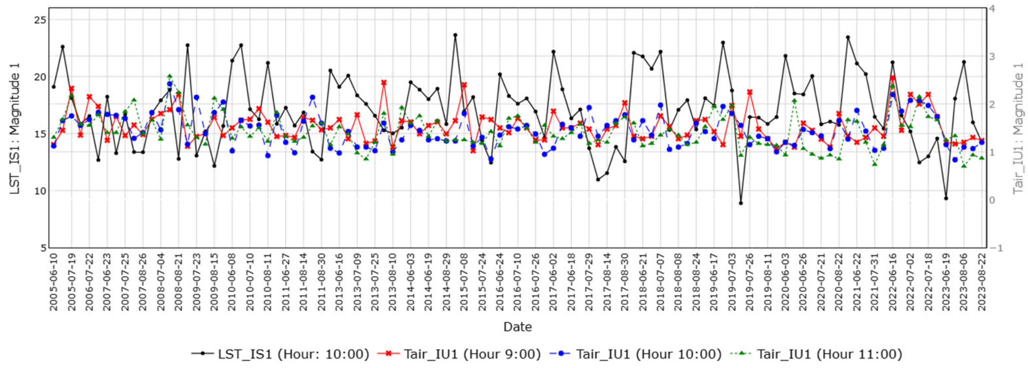

(**a**)

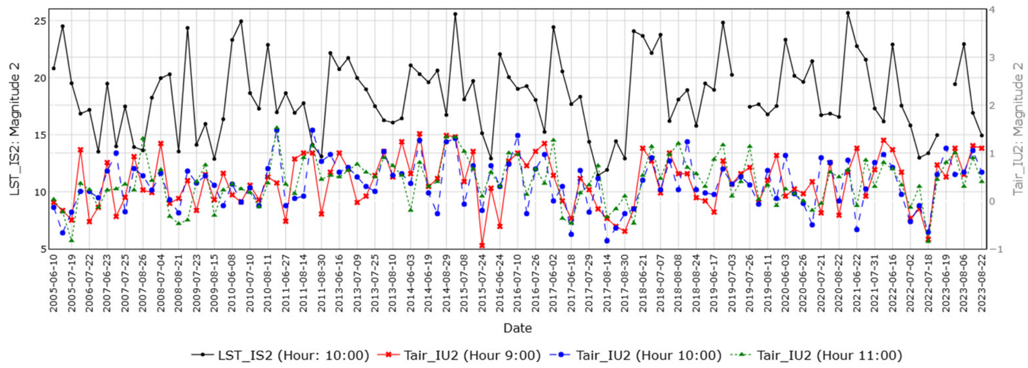

(**b**)

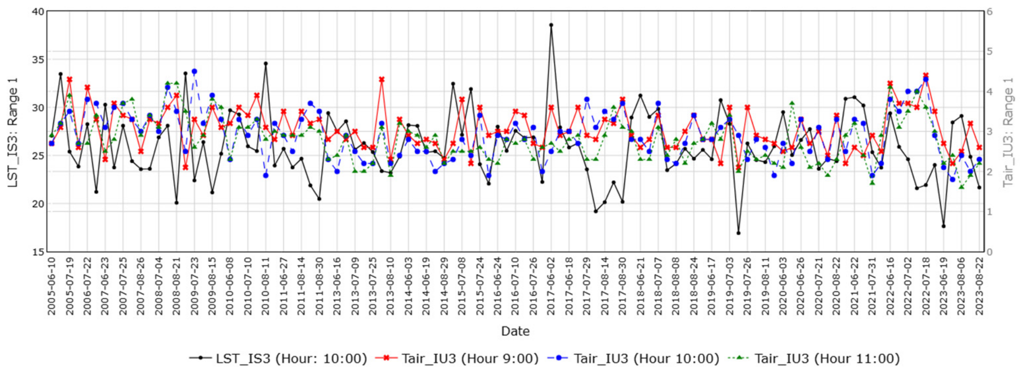

(**c**)

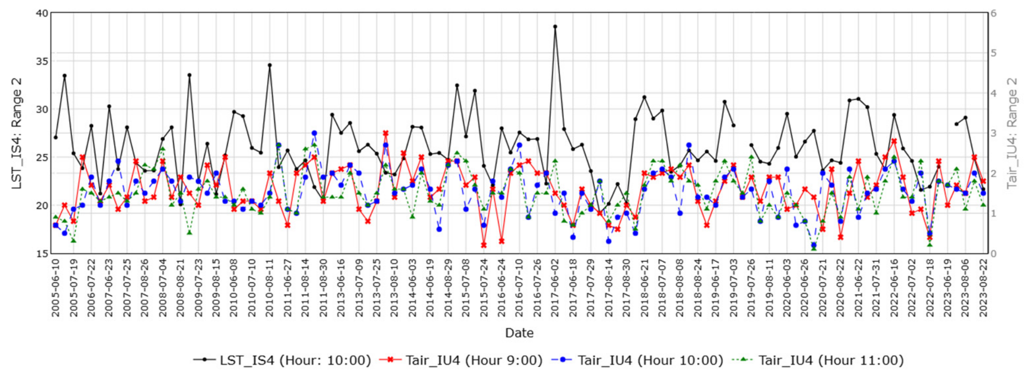

(**d**)

Figure 10. Comparison of daytime UHI and SUHI intensity indicators derived from LST and T_{air}. (**a**) Magnitude 1, (**b**) Magnitude 2, (**c**) Range 1, and (**d**) Range 2. LST is shown on the primary y-axis and T_{air} on the secondary y-axis at 09:00, 10:00 (Landsat overpass), and 11:00 UTC.

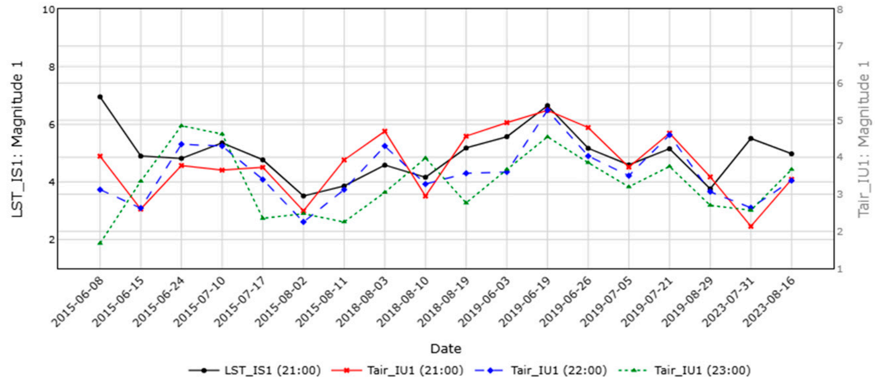

(a)

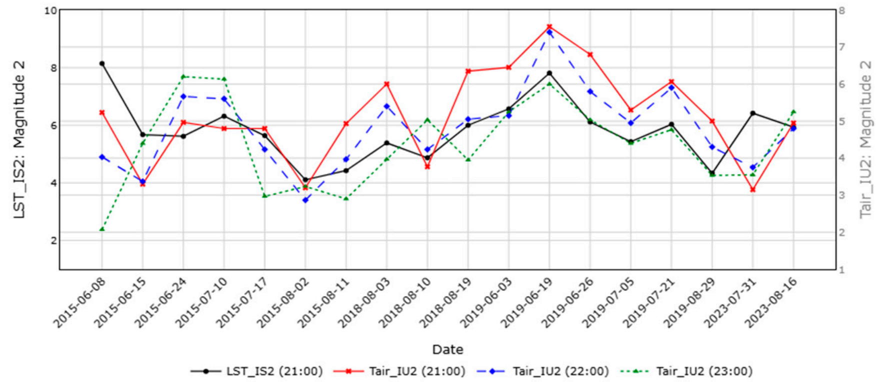

(b)

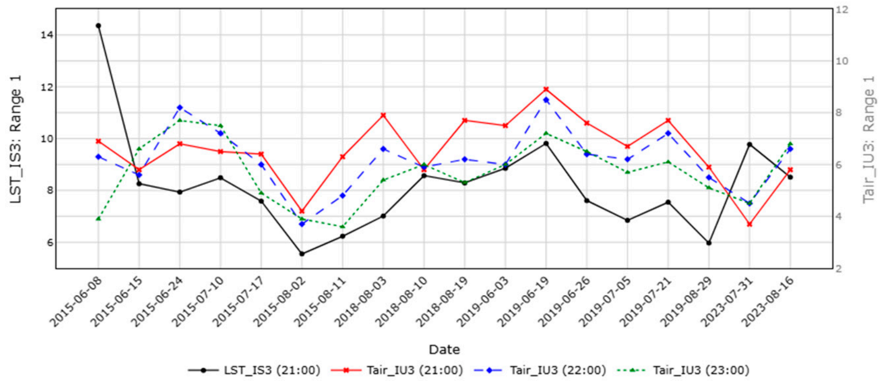

(c)

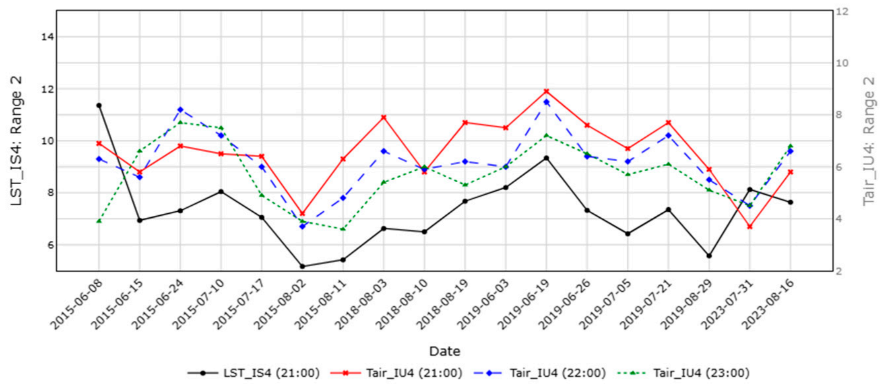

(d)

Figure 11. Comparison of nighttime UHI and SUHI intensity indicators derived from LST and T_{air}. (**a**) Magnitude 1, (**b**) Magnitude 2, (**c**) Range 1, and (**d**) Range 2. LST is shown on the primary y-axis and T_{air} on the secondary y-axis at 09:00, 10:00 (Landsat overpass), and 11:00 UTC.

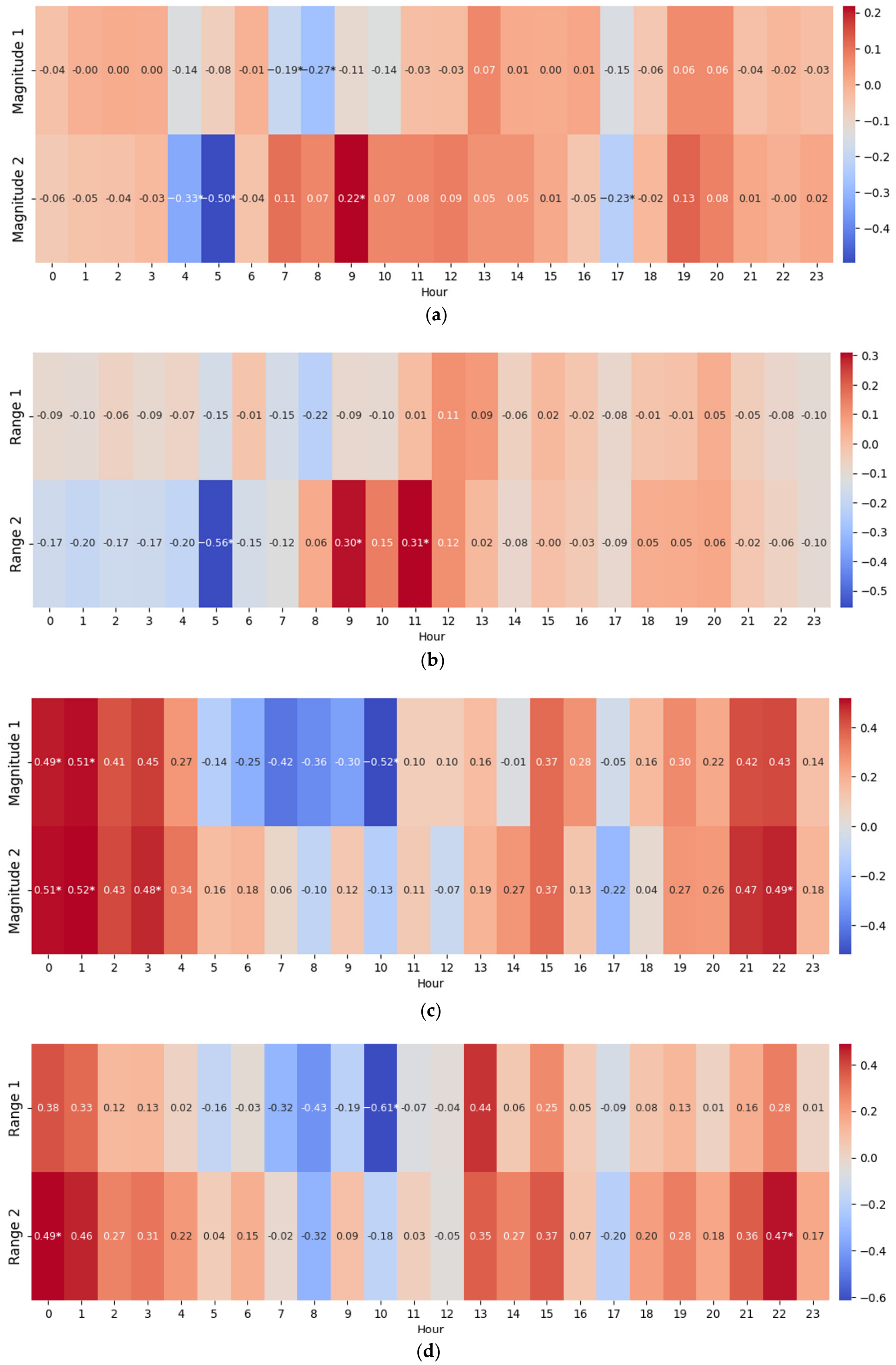

Figure 12. Daytime and nighttime cross-correlation heatmaps between UHI and SUHI intensity indicators. Panels (**a**,**b**) show the daytime results for the magnitude and range indicators, respectively, whereas panels (**c**,**d**) show the corresponding nighttime results. The asterisks indicate statistically significant correlations ($p < 0.05$).

For Magnitude 1 (Figure 12a), correlations remained generally weak throughout the day, fluctuating around zero, with slightly negative values during the early morning and late afternoon and only marginally positive values around midday.

Magnitude 2 showed a clearer diurnal pattern. Correlations were negative during the early morning, became positive from approximately 07:00 UTC, and reached their highest values in the late morning before weakening again during the afternoon. This pattern suggests a shift in the heat exchange dynamics between the surface and the atmosphere.

Range 1 (Figure 12b) showed consistently weak correlations, whereas Range 2 displayed a more pronounced diurnal cycle, with the strongest negative correlations before sunrise and the highest positive correlations during the late morning. Correlations declined again during the afternoon, reflecting the increasing influence of atmospheric processes.

For the nighttime analysis, Magnitude 1 (Figure 12c) showed its strongest positive correlations during the first part of the night, followed by a progressive decline toward the morning and then a recovery in the evening as the acquisition time approached.

Magnitude 2 exhibited the most stable behavior, maintaining positive correlations throughout most of the night and again around the Landsat overpass, indicating a persistent correspondence between nighttime LST and urban–rural Tair differences.

Among the range-based indices, Range 1 displayed only moderate agreement, whereas Range 2 showed the strongest relationship with nighttime LST. Correlations were highest during the early night, weakened during the morning, and increased again toward the evening, confirming a clear diurnal cycle in the coupling between nighttime LST and hourly Tair variations.

4. Discussion

4.1. Discussion of Urban–Rural LST and T_{air} Patterns

The observed summer LST increase is consistent with findings from other cities in the Po Valley and similar mid-latitude environments, where surface warming has been associated with land-use change, urban expansion, and increasing imperviousness [57,58]. Likewise, the daytime urban–rural LST differences observed in Modena fall within the range reported for medium-sized cities [59–61]. These patterns are consistent with the SUHI mechanism, whereby impervious materials store daytime solar energy and release it more slowly after sunset [2,60], explaining the stronger daytime than nighttime urban–rural contrast observed here.

The similar warming rates in urban and rural LST series suggest that regional atmospheric forcing acts in synergy with local urban drivers [62–64].

Land-use change supports this interpretation. Corine Land Cover data (1976–2020) [65] reveal that cultivable land decreased by 11.4% in the rural area and 4.1% in the urban area, while urban and industrial surfaces expanded by approximately 11% of the total municipal territory (183.5 km^2) (Figure S1). These changes reduced evapotranspirative cooling and increased LST in both areas, reinforcing the link between regional climate trends and local land cover change.

Given the proximity between the urban and rural sites, we verified the internal composition of the rural area using the Provincial Territorial Coordination Plan (PTCP) for the settlement system and rural territory [66]. Peri-urban agricultural land and settled built-up areas account for approximately 21% of the rural area (Table S1); excluding this fraction yielded LST trends nearly identical to the original classification, with differences of only 0.2–0.5 °C (Figure S2), providing further evidence that the urban–rural contrast is not substantially driven by peri-urban influence.

The nighttime peak around 2015, visible in both urban and rural LST series, likely reflects a major regional heat event, whereas the long-term upward trend is consistent

https://doi.org/10.3390/rs18162681

with the combined influence of regional climate warming and the land cover changes described above. The contrasting daytime and nighttime T_{air} behavior further emphasize the different mechanisms governing urban thermal conditions. The slightly higher daytime temperatures observed at the rural stations may reflect local land management conditions and the rapid heating of dry agricultural surfaces, whereas the significantly stronger nighttime T_{air} warming observed in the urban area is consistent with enhanced UHI development sustained by reduced nocturnal cooling and heat storage in the built environment [67]. The strong nighttime agreement between LST and T_{air} suggests a close coupling between surface and near-surface atmospheric thermal conditions, consistent with previous findings [54,68]. Compared to values reported for other Mediterranean cities (+0.02–0.05 °C yr^{-1}) [69], the nighttime rates observed in Modena are higher, likely reflecting the relatively short LST record and the occurrence of exceptionally hot summers during the study period. This could suggest an intensification of the nighttime SUHI; this interpretation should be confirmed using longer observational records.

4.2. Drivers of UHI and SUHI Intensity

The daytime indicator series (Figure 10) demonstrate that LST-based indices consistently exhibit larger amplitudes than their T_{air}-based counterparts. This difference reflects the contrasting thermal responses of urban surfaces and the lower atmosphere. Impervious materials such as asphalt, concrete, and brick respond rapidly to incoming solar radiation, reaching much higher temperatures than the overlying air, whereas T_{air} integrates atmospheric processes including turbulent mixing, convection, evapotranspiration, and local air circulation [54,70]. Consequently, the pronounced daytime surface thermal contrasts are only partially reflected in the corresponding atmospheric UHI intensity.

The comparison at 09:00, 10:00, and 11:00 UTC further indicates that the closest agreement between LST and T_{air} is not always centered exactly on the Landsat overpass time. This finding highlights the importance of examining multiple time windows when using satellite-derived LST as a proxy for near-surface T_{air} [30].

The nighttime indicators series (Figure 11) show that T_{air}-based variability can equal or even exceed the corresponding LST differences, particularly between 21:00 and 22:00 UTC. This behavior suggests that urban–rural atmospheric temperature contrasts may persist after surface cooling has begun, indicating a delayed atmospheric response relative to the satellite observation.

Overall, these results suggest that the relationship between SUHI and UHI depends strongly on the time of day. While daytime LST appears to primarily reflect the immediate thermal response of urban surfaces to solar heating, nighttime conditions seem to exhibit a stronger coupling between the surface and the lower atmosphere, which may allow Tair-based indicators to better capture the persistence of the urban heat island. This behavior is consistent with previous studies suggesting that nighttime LST better preserves the urban thermal signal [16].

4.3. Temporal Relationships Between UHI and SUHI

The cross-correlation analysis of the daytime dataset (Figure 12) shows that the 10:00 UTC LST snapshot is only weakly related to the hourly evolution of T_{air}-based indices. As discussed above, this reflects the different daytime response of surface and T_{air} to radiation, surface properties, and turbulent heat fluxes. In line with previous studies [5,71], the weak correlations suggest that daytime surface patterns do not translate directly into equivalent air temperature differences. Likewise, the negative correlations observed in the early morning further confirm that nighttime UHI dynamics are not adequately captured by daytime imagery, consistent with previous studies on the limits of single daytime acquisitions [4,72].

In contrast, the nighttime cross-correlation analysis (Figure 12) shows a clearer relationship between the 21:00 UTC LST snapshot and the hourly evolution of T_{air}-based indicators. The highest correlations during the evening and early nighttime hours indicate a closer coupling between surface and near-surface atmospheric thermal conditions, consistent with previous studies [73,74]. The decline during the morning transition indicates that the nocturnal signal does not extend linearly into daytime conditions because ventilation, mixing, and boundary layer changes rapidly modify urban–rural temperature differences [75,76].

Overall, the cross-correlation analysis demonstrates that the relationship between SUHI and UHI is strongly time dependent. Nighttime LST provides a more representative proxy of atmospheric UHI because of the stronger coupling between the surface and the lower atmosphere, whereas daytime LST primarily reflects the instantaneous thermal response of urban surfaces to solar forcing. These findings support the use of integrated surface–air observations and multi-temporal analyses to improve the characterization of urban thermal environments, particularly in medium-sized cities [77,78].

5. Limitations and Future Research Directions

Some limitations should be considered when interpreting the findings and identifying future research directions. First, the nighttime analysis is based on only 19 cloud-free Landsat scenes, providing a less comprehensive temporal record than the daytime dataset. Consequently, the nighttime results should be interpreted with caution and regarded as representative of the available observations rather than as a continuous long-term record. Moreover, daytime and nighttime analyses are based on clear-sky acquisitions collected at different times of day and over different years, thus representing thermal responses rather than continuous daily measurements. Because daytime and nighttime thermal conditions are governed by different physical processes, comparisons between them should be regarded as complementary rather than as direct quantitative equivalents. In addition, since LST represents an area-integrated pixel value, whereas T_{air} is measured at a specific location, their comparison is influenced by atmospheric conditions and the local characteristics surrounding the monitoring stations. The results may also be sensitive to station selection, the definition of urban and rural reference areas, and satellite acquisition timing.

These limitations suggest several directions for future research. A denser and more spatially robust monitoring network, together with a greater availability of nighttime thermal imagery, would improve the robustness of surface–air comparisons and the interpretation of thermal indicators. Future studies should also test the performance of these indicators across different climatic contexts, urban forms, and seasonal conditions while integrating information on vegetation dynamics and urban morphology, including Local Climate Zone (LCZ) classifications. From a policy perspective, the results support the need for continuous urban climate monitoring and for planning strategies aimed at reducing imperviousness, increasing vegetation cover, and improving ventilation and thermal resilience, particularly in medium-sized cities exposed to increasingly hot summer conditions.

6. Conclusions

This study highlights the multi-faceted nature of urban thermal dynamics, showing that LST and T_{air} observations acquired during the daytime and nighttime capture distinct but interconnected aspects of the UHI phenomenon. Daytime LST revealed persistent urban heat retention, with temperature differences of up to 6 °C, while nighttime warming confirmed a sustained urban excess LST of about 3 °C. Heatwave years, such as 2015, further amplified these patterns. Daytime LST also showed far greater spatial variability than T_{air}, exceeding 20–30 °C versus only 2–4 °C. Comparisons between nighttime T_{air} and LST trends showed very strong correlations (r = 0.96 in urban areas and r = 0.98 in rural areas), indicating a close link between surface and near-surface thermal behavior, although nighttime LST cooled faster than T_{air} after sunset.

Although nighttime LST and T_{air} were strongly correlated, daytime and nighttime LST trends specifically represent changes in surface thermal conditions under clear-sky conditions and should not be interpreted as direct estimates of long-term air temperature trends, which are governed by distinct atmospheric dynamics.

The analysis of Magnitude 1–2 and Range 1–2 further showed that nighttime LST (21:00 UTC) was more closely related to T_{air}, with correlations of 0.49, 0.51, and 0.52, whereas daytime LST (10:00 UTC) showed weaker or negative relationships. In line with previous studies, these results indicate that nighttime satellite observations better preserve the urban thermal signal under stable conditions, while daytime imagery is more affected by rapidly evolving atmospheric processes. Overall, this study confirms Modena as a valuable case study for UHI research among medium-sized cities and underscores the need for systematic daytime and nighttime observations to capture the full UHI cycle and improve urban climate assessment under ongoing climate change.

Supplementary Materials: The following supporting information can be downloaded at: https://www.mdpi.com/article/10.3390/rs18162681/s1. Figure S1: Land cover changes (%) between 1976 and 2020 in the urban and rural study areas of Modena, expressed as a percentage of the total study area; Figure S2: Comparison of summer LST trends for the original and refined rural study areas after excluding peri-urban and built-up land, * Full Rural = rural area excluding peri-urban and built-up land; Table S1: Land-use composition of the rural study area according to the Provincial Territorial Coordination Plan (PTCP).

Author Contributions: S.V.P.: Conceptualization; methodology; software; formal analysis; resources; data curation; writing—original draft; writing—review and editing. F.D.: Conceptualization; methodology; formal analysis; writing—review and editing. S.C.: Conceptualization; methodology; formal analysis; writing—review and editing. J.A.S.: Conceptualization; methodology; formal analysis; validation; writing—review and editing. L.D.l.F.D.: Software. S.T.: Writing—review and editing, supervision. All authors have read and agreed to the published version of the manuscript.

Funding: This research received no external funding.

Data Availability Statement: The LST datasets generated during the current study are available from the corresponding author upon reasonable request. The meteorological data used in the analysis are publicly available at https://simc.arpae.it/dext3r/ (accessed on 1 May 2025).

Acknowledgments: This paper and related research have been conducted during and with the support of the Italian interuniversity PhD course in Sustainable Development and Climate Change (SDC) (www.phd-sdc.it) (accessed on 12 March 2025). The authors wish to express their sincere gratitude to the Global Change Unit (UCG) Group at the University of Valencia, whose institutional support was instrumental to the development of this study. We also acknowledge the Istituto Nazionale di Geofisica e Vulcanologia (INGV) in Rome for their valuable collaboration.

Conflicts of Interest: Author Lucas de la Fuente Daruich was employed by the company Orbit. The remaining authors declare that the research was conducted in the absence of any commercial or financial relationships that could be construed as a potential conflict of interest.

References

1. Aghazadeh, F.; Rahimi, A.; Tarashkar, M.; Firozjaei, M.K.; Ioja, C.; Ondrejicka, V.; Finka, M. Assessing the Green Infrastructure and Built up Effects in Enhancing Thermal Comfort for Vulnerable Populations in Urban Heat Waves: A Case Study of Tabriz Metropolitan. *Remote Sens. Appl. Soc. Environ.* **2025**, *39*, 101671. [CrossRef]

2. Gupta, A.; De, B.; Feng, Z. Intra-City Disparities in Urban Green Space Proximity and Its Association with Infrastructures and Demography. *Remote Sens. Appl. Soc. Environ.* **2025**, *39*, 101724. [CrossRef]
3. Mohajerani, A.; Bakaric, J.; Jeffrey-Bailey, T. The Urban Heat Island Effect, Its Causes, and Mitigation, with Reference to the Thermal Properties of Asphalt Concrete. *J. Environ. Manag.* **2017**, *197*, 522–538. [CrossRef] [PubMed]
4. Voogt, J.A.; Oke, T.R. Thermal Remote Sensing of Urban Climates. *Remote Sens. Environ.* **2003**, *86*, 370–384. [CrossRef]
5. Weng, Q. Thermal Infrared Remote Sensing for Urban Climate and Environmental Studies: Methods, Applications, and Trends. *ISPRS J. Photogramm. Remote Sens.* **2009**, *64*, 335–344. [CrossRef]
6. Onačillová, K.; Fedor, T.; Gallay, M.; Šašak, J.; Bogľarský, J.; Kaňuk, J.; Salajová, N. Local Climate Zones and Diurnal Surface Heating in a Central European City: A Comparison of Landsat, ECOSTRESS, and ENVI-Met with in Situ Measurements in Košice (Slovakia). *Remote Sens. Appl. Soc. Environ.* **2026**, *41*, 101933. [CrossRef]
7. Shaker, R.R.; Altman, Y.; Deng, C.; Vaz, E.; Forsythe, K.W. Investigating Urban Heat Island through Spatial Analysis of New York City Streetscapes. *J. Clean. Prod.* **2019**, *233*, 972–992. [CrossRef]
8. Zhang, X.; Estoque, R.C.; Murayama, Y.; Ranagalage, M. Capturing Urban Heat Island Formation in a Subtropical City of China Based on Landsat Images: Implications for Sustainable Urban Development. *Environ. Monit. Assess.* **2021**, *193*, 130. [CrossRef] [PubMed]
9. Dimoudi, A.; Zoras, S.; Kantzioura, A.; Stogiannou, X.; Kosmopoulos, P.; Pallas, C. Use of Cool Materials and Other Bioclimatic Interventions in Outdoor Places in Order to Mitigate the Urban Heat Island in a Medium Size City in Greece. *Sustain. Cities Soc.* **2014**, *13*, 89–96. [CrossRef]
10. Xie, Z.Q.; Du, Y.; Miao, Q.; Zhang, L.L.; Wang, N. An Approach to Characterizing the Spatial Pattern and Scale of Regional Heat Islands Over Urban Agglomerations. *Geophys. Res. Lett.* **2022**, *49*, e2022GL099117. [CrossRef]
11. Oke, T.R. The Energetic Basis of the Urban Heat Island. *Q. J. R. Meteorol. Soc.* **1982**, *108*, 1–24. [CrossRef]
12. Tomlinson, C.J.; Chapman, L.; Thornes, J.E.; Baker, C.J. Derivation of Birmingham's Summer Surface Urban Heat Island from MODIS Satellite Images. *Int. J. Climatol.* **2012**, *32*, 214–224. [CrossRef]
13. Chakraborty, S.D.; Kant, Y.; Mitra, D. Assessment of Land Surface Temperature and Heat Fluxes over Delhi Using Remote Sensing Data. *J. Environ. Manag.* **2015**, *148*, 143–152. [CrossRef] [PubMed]
14. Welegedara, N.P.Y.; Agrawal, S.K.; Lotfi, G. Exploring Spatiotemporal Changes of the Urban Heat Island Effect in High-Latitude Cities at a Neighbourhood Level: A Case of Edmonton, Canada. *Sustain. Cities Soc.* **2023**, *90*, 104403. [CrossRef]
15. Park, K.; Jin, H.-G.; Baik, J.-J. Contrasting Interactions between Urban Heat Islands and Heat Waves in Seoul, South Korea, and Their Associations with Synoptic Patterns. *Urban Clim.* **2023**, *49*, 101524. [CrossRef]
16. Zargari, M.; Mofidi, A.; Entezari, A.; Baaghideh, M. Climatology of Tehran Surface Heat Island: A Satellite-Based Spatial Analysis. *Sci. Rep.* **2025**, *15*, 10567. [CrossRef] [PubMed]
17. Alghamdi, A.S. An Integrated ML-Powered Geospatial Analysis of Surface Urban Heat Island and Its Mitigation in Riyadh City, Saudi Arabia. *Urban Clim.* **2025**, *64*, 102642. [CrossRef]
18. Olgun, R.; Karakuş, N.; Selim, S.; Yilmaz, T.; Erdoğan, R.; Aklıbaşında, M.; Dönmez, B.; Çakır, M.; Ardahanlıoğlu, Z.R. Impacts of Landscape Composition on Land Surface Temperature in Expanding Desert Cities: A Case Study in Arizona, USA. *Land* **2025**, *14*, 1274. [CrossRef]
19. Noro, M.; Lazzarin, R. Urban Heat Island in Padua, Italy: Simulation Analysis and Mitigation Strategies. *Urban Clim.* **2015**, *14*, 187–196. [CrossRef]
20. Martinelli, A.; Kolokotsa, D.-D.; Fiorito, F. Urban Heat Island in Mediterranean Coastal Cities: The Case of Bari (Italy). *Climate* **2020**, *8*, 79. [CrossRef]
21. Semenzato, P.; Bortolini, L. Urban Heat Island Mitigation and Urban Green Spaces: Testing a Model in the City of Padova (Italy). *Land* **2023**, *12*, 476. [CrossRef]
22. Zauli Sajani, S.; Marchesi, S.; Lauriola, P.; Tomozeiu, R.; Botarelli, L.; Bonafè, G.; Guaragno, G.; Fiumi, F.; Zanelli, M.; Gherardi, L. UHI in the Metropolitan Cluster of Bologna-Modena: Mitigation and Adaptation Strategies. In *Counteracting Urban Heat Island Effects in a Global Climate Change Scenario*; Springer: Cham, Switzerland, 2016; pp. 131–200.
23. Barbieri, T.; Despini, F.; Teggi, S. A Multi-Temporal Analyses of Land Surface Temperature Using Landsat-8 Data and Open Source Software: The Case Study of Modena, Italy. *Sustainability* **2018**, *10*, 1678. [CrossRef]
24. Zullo, F.; Fazio, G.; Romano, B.; Marucci, A.; Fiorini, L. Effects of Urban Growth Spatial Pattern (UGSP) on the Land Surface Temperature (LST): A Study in the Po Valley (Italy). *Sci. Total Environ.* **2019**, *650*, 1740–1751. [CrossRef] [PubMed]
25. Despini, F.; Ferrari, C.; Santunione, G.; Tommasone, S.; Muscio, A.; Teggi, S. Urban Surfaces Analysis with Remote Sensing Data for the Evaluation of UHI Mitigation Scenarios. *Urban Clim.* **2021**, *35*, 100761. [CrossRef]
26. Costanzini, S.; Boccolari, M.; Vega Parra, S.; Despini, F.; Lombroso, L.; Teggi, S. A Comparative Analysis of Temperature Trends at Modena Geophysical Observatory and Mount Cimone Observatory, Italy. *Int. J. Climatol.* **2024**, *44*, 4741–4766. [CrossRef]

27. Ali, J.M.; Marsh, S.H.; Smith, M.J. A Comparison between London and Baghdad Surface Urban Heat Islands and Possible Engineering Mitigation Solutions. *Sustain. Cities Soc.* **2017**, *29*, 159–168. [CrossRef]
28. Colaninno, N. Insights into Heat Islands at the Regional Scale Using a Data-Driven Approach. *City Environ. Interact.* **2023**, *20*, 100124. [CrossRef]
29. Zhou, D.; Xiao, J.; Bonafoni, S.; Berger, C.; Deilami, K.; Zhou, Y.; Frolking, S.; Yao, R.; Qiao, Z.; Sobrino, J.A. Satellite Remote Sensing of Surface Urban Heat Islands: Progress, Challenges, and Perspectives. *Remote Sens.* **2019**, *11*, 48. [CrossRef]
30. Yang, C.; Yan, F.; Zhang, S. Comparison of Land Surface and Air Temperatures for Quantifying Summer and Winter Urban Heat Island in a Snow Climate City. *J. Environ. Manag.* **2020**, *265*, 110563. [CrossRef] [PubMed]
31. Sheng, L.; Tang, X.; You, H.; Gu, Q.; Hu, H. Comparison of the Urban Heat Island Intensity Quantified by Using Air Temperature and Landsat Land Surface Temperature in Hangzhou, China. *Ecol. Indic.* **2017**, *72*, 738–746. [CrossRef]
32. Peel, M.C.; Finlayson, B.L.; McMahon, T.A. Updated World Map of the Köppen-Geiger Climate Classification. *Hydrol. Earth Syst. Sci.* **2007**, *11*, 1633–1644. [CrossRef]
33. Comune di Modena. Demografia. Available online: https://www.comune.modena.it/argomenti/statistica/demografia (accessed on 6 May 2025).
34. Du, L.; Zhou, T.; Li, M.S.; Gong, D.Y. Urban Heat Island Effects Derived from Dense Landsat Thermal Observations in Nanjing, China. *IOP Conf. Ser. Earth Environ. Sci.* **2014**, *17*, 012162. [CrossRef]
35. European Environment Agency. CORINE Land Cover 2018 (Raster 100m). Available online: https://sdi.eea.europa.eu/catalogue/geoss/api/records/960998c1-1870-4e82-8051-6485205ebbac (accessed on 20 March 2026).
36. Sobrino, J.A.; Irakulis, I. A Methodology for Comparing the Surface Urban Heat Island in Selected Urban Agglomerations Around the World from Sentinel-3 SLSTR Data. *Remote Sens.* **2020**, *12*, 2052. [CrossRef]
37. de Almeida, C.R.; Garcia, N.; Campos, J.C.; Alírio, J.; Arenas-Castro, S.; Gonçalves, A.; Sillero, N.; Teodoro, A.C. Time-Series Analyses of Land Surface Temperature Changes with Google Earth Engine in a Mountainous Region. *Heliyon* **2023**, *9*, e18846. [CrossRef] [PubMed]
38. Dewa, D.D.; Buchori, I.; Sejati, A.W.; Liu, Y. Integrating Google Earth Engine and Regional Ecological Corridor Modeling for Remote Sensing-Based Urban Heat Island Mitigation in Java, Indonesia. *Remote Sens. Appl. Soc. Environ.* **2025**, *38*, 101573. [CrossRef]
39. Maulana, J.; Bioresita, F. Monitoring of Land Surface Temperature in Surabaya, Indonesia from 2013–2021 Using Landsat-8 Imagery and Google Earth Engine. *IOP Conf. Ser. Earth Environ. Sci.* **2023**, *1127*, 012027. [CrossRef]
40. Roy, B.; Bari, E. Examining the Relationship between Land Surface Temperature and Landscape Features Using Spectral Indices with Google Earth Engine. *Heliyon* **2022**, *8*, e10668. [CrossRef] [PubMed]
41. USGS. Landsat 8–9 Collection 2 Level 2 Science Product Guide. 2024. Available online: https://www.usgs.gov/media/files/landsat-8-9-collection-2-level-2-science-product-guide (accessed on 10 January 2025).
42. USGS. Landsat 4–7 Collection 2 Level 2 Science Product Guide. 2021. Available online: https://www.usgs.gov/media/files/landsat-4-7-collection-2-level-2-science-product-guide (accessed on 10 January 2025).
43. Lauer, M.; Aswani, S. Integrating Indigenous Ecological Knowledge and Multi-Spectral Image Classification for Marine Habitat Mapping in Oceania. *Ocean Coast. Manag.* **2008**, *51*, 495–504. [CrossRef]
44. USGS. Landsat 7 Scan Line Corrector (SLC) Failure. 2024. Available online: https://www.usgs.gov/landsat-missions/landsat-7 (accessed on 12 February 2025).
45. Zhu, Z.; Woodcock, C.E. Object-Based Cloud and Cloud Shadow Detection in Landsat Imagery. *Remote Sens. Environ.* **2012**, *118*, 83–94. [CrossRef]
46. Schmidt, G.; Jenkerson, C.B.; Masek, J.; Vermote, E.; Gao, F. *Landsat Ecosystem Disturbance Adaptive Processing System (LEDAPS) Algorithm Description*; U.S. Geological Survey: Reston, VA, USA, 2013.
47. Silvestri, M.; Romaniello, V.; Hook, S.; Musacchio, M.; Teggi, S.; Buongiorno, M.F. First Comparisons of Surface Temperature Estimations between ECOSTRESS, ASTER and Landsat 8 over Italian Volcanic and Geothermal Areas. *Remote Sens.* **2020**, *12*, 184. [CrossRef]
48. Sekertekin, A.; Bonafoni, S. Sensitivity Analysis and Validation of Daytime and Nighttime Land Surface Temperature Retrievals from Landsat 8 Using Different Algorithms and Emissivity Models. *Remote Sens.* **2020**, *12*, 2776. [CrossRef]
49. Arpae. Arpae Emilia-Romagna, Dext3r. Available online: https://simc.arpae.it/dext3r/ (accessed on 29 October 2024).
50. Sobrino, J.A.; Jiménez-Muñoz, J.C.; Paolini, L. Land Surface Temperature Retrieval from LANDSAT TM 5. *Remote Sens. Environ.* **2004**, *90*, 434–440. [CrossRef]
51. Jimenez Munoz, J.C.; Cristobal, J.; Sobrino, J.A.; Soria, G.; Ninyerola, M.; Pons, X. Revision of the Single-Channel Algorithm for Land Surface Temperature Retrieval From Landsat Thermal-Infrared Data. *IEEE Trans. Geosci. Remote Sens.* **2009**, *47*, 339–349. [CrossRef]

52. Li, Z.-L.; Wu, H.; Wang, N.; Qiu, S.; Sobrino, J.A.; Wan, Z.; Tang, B.-H.; Yan, G. Land Surface Emissivity Retrieval from Satellite Data. *Int. J. Remote Sens.* **2013**, *34*, 3084–3127. [CrossRef]
53. Jiménez-Muñoz, J.C.; Sobrino, J.A.; Skoković, D.; Mattar, C.; Cristóbal, J. Land Surface Temperature Retrieval Methods from Landsat-8 Thermal Infrared Sensor Data. *IEEE Geosci. Remote Sens. Lett.* **2014**, *11*, 1840–1843. [CrossRef]
54. Schwarz, N.; Schlink, U.; Franck, U.; Großmann, K. Relationship of Land Surface and Air Temperatures and Its Implications for Quantifying Urban Heat Island Indicators—An Application for the City of Leipzig (Germany). *Ecol. Indic.* **2012**, *18*, 693–704. [CrossRef]
55. Russo, S.; Sillmann, J.; Fischer, E.M. Top Ten European Heatwaves since 1950 and Their Occurrence in the Coming Decades. *Environ. Res. Lett.* **2015**, *10*, 124003. [CrossRef]
56. Bionda, A.; Cortellari, M.; Negro, A.; Crepaldi, P. 70 Years of Heat Waves and Summer Climate Change Affecting Italian Small Ruminant Populations. *Pastor. Res. Policy Pract.* **2024**, *14*, 12848. [CrossRef]
57. Rao, P.; Tassinari, P.; Torreggiani, D. Exploring the Land-Use Urban Heat Island Nexus under Climate Change Conditions Using Machine Learning Approach: A Spatio-Temporal Analysis of Remotely Sensed Data. *Heliyon* **2023**, *9*, e18423. [CrossRef] [PubMed]
58. Trotter, L.; Dewan, A.; Robinson, T. Effects of Rapid Urbanisation on the Urban Thermal Environment between 1990 and 2011 in Dhaka Megacity, Bangladesh. *AIMS Environ. Sci.* **2017**, *4*, 145–167. [CrossRef]
59. Stathopoulou, M.; Cartalis, C. Daytime Urban Heat Islands from Landsat ETM+ and Corine Land Cover Data: An Application to Major Cities in Greece. *Sol. Energy* **2007**, *81*, 358–368. [CrossRef]
60. Bounoua, L.; Zhang, P.; Mostovoy, G.; Thome, K.; Masek, J.; Imhoff, M.; Shepherd, M.; Quattrochi, D.; Santanello, J.; Silva, J.; et al. Impact of Urbanization on US Surface Climate. *Environ. Res. Lett.* **2015**, *10*, 084010. [CrossRef]
61. Abulibdeh, A. Analysis of Urban Heat Island Characteristics and Mitigation Strategies for Eight Arid and Semi-Arid Gulf Region Cities. *Environ. Earth Sci.* **2021**, *80*, 259. [CrossRef] [PubMed]
62. Anniballe, R.; Bonafoni, S.; Pichierri, M. Spatial and Temporal Trends of the Surface and Air Heat Island over Milan Using MODIS Data. *Remote Sens. Environ.* **2014**, *150*, 163–171. [CrossRef]
63. Orusa, T.; Mondino, E.B. Landsat 8 Thermal Data to Support Urban Management and Planning in the Climate Change Era: A Case Study in Torino Area, NW Italy. In *Proceedings of the Remote Sensing Technologies and Applications in Urban Environments IV*; SPIE: Bellingham, WA, USA, 2019; Volume 11157, pp. 133–149.
64. Morabito, M.; Crisci, A.; Guerri, G.; Messeri, A.; Congedo, L.; Munafò, M. Surface Urban Heat Islands in Italian Metropolitan Cities: Tree Cover and Impervious Surface Influences. *Sci. Total Environ.* **2021**, *751*, 142334. [CrossRef] [PubMed]
65. Regione Emilia-Romagna. Database Uso del Suolo. Available online: https://geoportale.regione.emilia-romagna.it/approfondimenti/database-uso-del-suolo (accessed on 28 July 2026).
66. Provincia di Modena. Cartografia di Piano. Available online: https://www.provincia.modena.it/temi-e-funzioni/territorio/pianificazione-territoriale-e-difesa-del-suolo/p-t-c-p/p-t-c-p-approvato/elaborati-cartografici-in-formato-shape-file/cartografia-di-piano/ (accessed on 28 July 2026).
67. Wei, L.; Sobrino, J.A. Surface Urban Heat Island Analysis Based on Local Climate Zones Using ECOSTRESS and Landsat Data: A Case Study of Valencia City (Spain). *Int. J. Appl. Earth Obs. Geoinf.* **2024**, *130*, 103875. [CrossRef]
68. Della-Marta, P.M.; Luterbacher, J.; von Weissenfluh, H.; Xoplaki, E.; Brunet, M.; Wanner, H. Summer Heat Waves over Western Europe 1880–2003, Their Relationship to Large-Scale Forcings and Predictability. *Clim. Dyn.* **2007**, *29*, 251–275. [CrossRef]
69. Polydoros, A.; Mavrakou, T.; Cartalis, C. Quantifying the Trends in Land Surface Temperature and Surface Urban Heat Island Intensity in Mediterranean Cities in View of Smart Urbanization. *Urban Sci.* **2018**, *2*, 16. [CrossRef]
70. Naserikia, M.; Hart, M.A.; Nazarian, N.; Bechtel, B.; Lipson, M.; Nice, K.A. Land Surface and Air Temperature Dynamics: The Role of Urban Form and Seasonality. *Sci. Total Environ.* **2023**, *905*, 167306. [CrossRef] [PubMed]
71. Chudnovsky, A.; Ben-Dor, E.; Saaroni, H. Diurnal Thermal Behavior of Selected Urban Objects Using Remote Sensing Measurements. *Energy Build.* **2004**, *36*, 1063–1074. [CrossRef]
72. Arnfield, A.J. Two Decades of Urban Climate Research: A Review of Turbulence, Exchanges of Energy and Water, and the Urban Heat Island. *Int. J. Climatol.* **2003**, *23*, 1–26. [CrossRef]
73. Sobrino, J.A.; Oltra-Carrió, R.; Sòria, G.; Bianchi, R.; Paganini, M. Impact of Spatial Resolution and Satellite Overpass Time on Evaluation of the Surface Urban Heat Island Effects. *Remote Sens. Environ.* **2012**, *117*, 50–56. [CrossRef]
74. Sobrino, J.A.; Oltra-Carrió, R.; Sòria, G.; Jiménez-Muñoz, J.C.; Franch, B.; Hidalgo, V.; Mattar, C.; Julien, Y.; Cuenca, J.; Romaguera, M.; et al. Evaluation of the Surface Urban Heat Island Effect in the City of Madrid by Thermal Remote Sensing. *Int. J. Remote Sens.* **2013**, *34*, 3177–3192. [CrossRef]
75. Masson, V. Urban Surface Modeling and the Meso-Scale Impact of Cities. *Theor. Appl. Climatol.* **2006**, *84*, 35–45. [CrossRef]
76. Schwaab, J. Sprawl or Compactness? How Urban Form Influences Urban Surface Temperatures in Europe. *City Environ. Interact.* **2022**, *16*, 100091. [CrossRef]

77. Kporha, V.K.; Fox, D.M.; Banitalebi, M.; Bouroubi, Y.; Fournier, R. Comparing Daily and 8-Day MODIS Land Surface Temperature Data for Urban Heat Island Assessment Using Random Forest Modeling in Data-Limited Regions. *Remote Sens. Appl. Soc. Environ.* **2026**, *41*, 101904. [CrossRef]
78. Li, S.; Li, W.; Yu, M.; Chen, D.; Xu, M.; Ren, M.; Yang, X. Urban Three-Dimension Green Quantity Estimation: An Approach Utilizing UAV, Satellite Imagery, and Machine Learning. *Remote Sens. Appl. Soc. Environ.* **2025**, *39*, 101691. [CrossRef]